

**Regional characteristics of variability in the Northern Hemisphere wintertime polar front
jet and subtropical jet in observations and CMIP6 models**

Xinhuiyu Liu¹, Kevin M. Grise¹, Daniel F. Schmidt¹, Robert E. Davis¹

¹ Department of Environmental Sciences, University of Virginia, Charlottesville, VA, USA

Corresponding author: Xinhuiyu Liu (xl7pd@virginia.edu)

Key Points:

- Northern Hemisphere wintertime polar front jet variability is associated with surface baroclinicity anomalies, except over the Pacific.
- Pacific tropical convection anomalies are linked to variations of the Northern Hemisphere wintertime subtropical jet at most longitudes.
- Tropical convection in CMIP6 models is often displaced westward when compared to observations, reflecting a climatological bias.

Abstract

Variability in the position and strength of the subtropical jet (STJ) and polar front jet (PFJ) streams has important implications for global and regional climate. Previous studies have related the position and strength of the STJ to tropical thermodynamic processes, whereas the position and strength of the PFJ are more associated with mid-latitude eddies. These conclusions have largely resulted from studies using idealized models.

In this study, ERA-Interim reanalysis and CMIP6 global climate models are used to examine month-to-month and interannual variability of the wintertime Northern Hemisphere (NH) STJ and PFJ. This study particularly focuses on the regional characteristics of the jet variability, extending previous studies on zonal-mean jet streams. Consistent with idealized modeling studies, a close relationship is found between tropical outgoing longwave radiation (OLR) and the STJ, and between mid-latitude surface temperature gradients and the PFJ. Variations of both jets are also linked to well-known teleconnection patterns.

Variations in tropical convection over the Pacific Ocean are associated with variations of the NH STJ at most longitudes, with different phases of the El Niño-Southern Oscillation (ENSO) associated with the shift and strengthening of the STJ in different regions. CMIP6 models generally capture these relationships, but the models' tropical convection is often displaced westward when compared to observations, reflecting a climatological bias in OLR in the western tropical Pacific Ocean in many models. The displaced tropical convection in models excites different paths of Rossby wave propagation, resulting in different ENSO teleconnections on the STJ over North America and Europe.

1. Introduction

Jet streams are relatively narrow bands of strong west-to-east winds in the upper troposphere. In the zonal mean climatology, there are two jet streams, the subtropical jet (STJ) and polar front jet (PFJ), located in both the Northern Hemisphere (NH) and Southern Hemisphere (SH). The STJ is commonly viewed as being driven by the angular momentum conservation in the poleward flowing upper tropospheric branch of the tropical Hadley circulation (Held & Hou, 1980; Schneider, 1977), and thus it is located near the poleward edge of Hadley Cell in each hemisphere. The PFJ is driven by the convergence of momentum by transient midlatitude eddies (Held, 1975; Panetta, 1993) and is consequently located at mid-latitudes where baroclinic instability is strongest.

This simple picture of the two jet streams, however, does not apply at all longitudes and in all seasons. For example, in the NH wintertime climatology, there are clearly two distinct jets in Eurasia, the Eastern Pacific Ocean, and the North Atlantic Ocean, while the STJ and PFJ are merged into a single jet stream in East Asia, the Western Pacific Ocean, and the Eastern United States (Christenson, Martin, & Handlos, 2017; Eichelberger & Hartmann, 2007; Koch, Wernli, & Davies, 2006; C. Li & Wettstein, 2012). The strength of the two jets also varies by region, with both the STJ and PFJ usually strongest over the Pacific Ocean during winter (Archer & Caldeira, 2008; Koch et al., 2006). The NH jet streams are weaker and further poleward during summer months (Archer and Caldeira 2008; Koch et al. 2006; Woollings et al. 2014). In the Southern Hemisphere (SH), a single jet stream is observed during summer, whereas somewhat more distinct subtropical and polar front jets are observed during winter (Bals-Elsholz et al., 2001; Kim & Lee, 2004)

The positions and strengths of the jets are not constant in time and vary from month to month and from year to year. Understanding variability in the position and strength of the jet streams is important, as it directly influences impactful surface weather events, such as extratropical cyclone tracks (Dickson and Namias 1976; Athanasiadis et al. 2010), blocking anticyclone frequency (Kaas and Branstator 1993; Barnes and Hartmann 2010; Woollings et al. 2018), heatwaves and cold air outbreaks (Mahlstein, Martius, Chevalier, & Ginsbourger, 2012; Petoukhov, Rahmstorf, Petri, & Schellnhuber, 2013), and atmospheric rivers and their associated heavy precipitation events (Ryoo et al., 2013; Zhang & Villarini, 2018). Previous studies have documented relationships between variability in the jet streams and known teleconnection patterns, including but not limited to the El Niño-Southern Oscillation (ENSO), the Northern Annular Mode (NAM)/North Atlantic Oscillation (NAO), the Pacific-North American teleconnection pattern (PNA), and the Southern Annular Mode (SAM). Variability in the PFJ is closely tied to the NAM/NAO, PNA, and SAM (Gallego et al., 2005; Strong & Davis, 2008; Woollings et al., 2014; Woollings et al., 2010), whereas variability in the STJ is expected to correlate with ENSO (Gallego et al., 2005; Lu, Chen, & Frierson, 2008; Seager et al., 2003). Jet streams, of course, also vary with synoptic weather systems on daily timescales (Handlos & Martin, 2016; Winters & Martin, 2016), but in this study, we focus on month-to-month and interannual variability of the two jet streams.

Whether the STJ and PFJ are merged together or in two distinct branches may also have important implications for global and regional climate. One example is the relative minimum in North Pacific storm track activity that occurs during mid-winter (January and February), even though the baroclinicity is the strongest during these months (Nakamura, 1992). A similar feature occurs in the North Atlantic storm track during years with a strong STJ (Afargan &

Kaspi, 2017). Several recent studies have attributed the existence of a mid-winter storm track minimum to the merging of the STJ and PFJ (Yuval et al. 2018; Novak et al. 2020). Previous studies have used idealized models to explain the merging and splitting of the two jets. Lee and Kim (2003) found that, when the STJ is relatively weak, the most favorable region for baroclinic wave growth often lies in midlatitudes, establishing an eddy-driven PFJ that is well separated from the STJ. In contrast, when the STJ is relatively strong, baroclinic wave growth occurs close enough to the STJ so that a single merged jet evolves. Son and Lee (2005) further found that a single merged jet forms preferentially when tropical heating is strong, while a double-jet state forms when tropical heating is weak enough to allow midlatitude eddies to grow more poleward and form a separate eddy-driven jet. Yuval and Kaspi (2018) concluded that baroclinic eddies are stronger when there is a strong distinct PFJ and are weaker when there is a merged jet.

These idealized model results provide insight into the processes that control the variability of the polar front and subtropical jets, but they are not entirely consistent with the jet characteristics found in observations or comprehensive global climate models. Based on the results of Lee and Kim (2003), one might expect that the positions and strengths of the STJ and PFJ are negatively correlated. That is, when the STJ is weak and equatorward, there should be a strong and poleward PFJ. However, several recent studies have found that interannual variability in the position and strength of the jets is only weakly correlated in the zonal mean (Davis & Birner, 2016, 2017; Menzel et al., 2019; Solomon et al., 2016; Waugh et al., 2018). To our knowledge, apart from a recent study on the SH jets in the Indo-Pacific sector (Gillett et al., 2021), the relationship between the interannual variability in the position and strength of the jets has not been examined in detail at individual longitudes.

106 The purpose of this study is to better understand the month-to-month and interannual
107 variability in the position and strength of the STJ and PFJ at individual longitudes. To do this,
108 we define the position and strength of polar front and subtropical jets using both reanalysis data
109 and global climate models. For this study, we focus our analysis on the wintertime (December–
110 February) jets in the NH because longitudinal asymmetries are much greater in the NH and the
111 jets are strongest in the winter season when the pole-to-equator temperature gradient is largest.
112 We find that variations in (1) tropical convective heating and (2) horizontal surface temperature
113 gradients at midlatitudes are closely linked to the month-to-month and interannual variations in
114 the position and intensity of the NH wintertime jet streams. Tropical convective heating is
115 closely linked to variations in the location and strength of the NH wintertime STJ, consistent
116 with the idealized modeling studies discussed above (Lee & Kim, 2003; Son & Lee, 2005),
117 observations associated with the El Niño-Southern Oscillation (Gallego et al., 2005; Lu et al.,
118 2008), and case studies of synoptic-scale weather events (Handlos & Martin, 2016; Winters &
119 Martin, 2016). Variations in surface baroclinicity are closely linked to variations in the location
120 and strength of the NH wintertime PFJ (see also Brayshaw et al. 2008; Sampe et al. 2010; Hall et
121 al. 2015).

122 The paper is organized as follows. Section 2 describes the data and methods used in this
123 study. Section 3 examines the wintertime variability in STJ and PFJ position and strength in
124 observations, and their linkages to tropical convective heating and midlatitude horizontal surface
125 temperature gradients. Section 4 explores the causes of model biases in these relationships.
126 Section 5 concludes with a discussion and summary of the results.

2. Data and Methods

2.1 Data

To examine observed wintertime variability in the jets, we use monthly-mean December–February zonal wind and surface temperature data from the European Centre for Medium-Range Weather Forecasts (ECMWF) Interim reanalysis data set (ERA-Interim; Dee et al., 2011). The data are provided at a spatial resolution of 0.75 degrees latitude \times 0.75 degrees longitude. We also make use of monthly-mean outgoing longwave radiation (OLR) data from the National Oceanic and Atmospheric Administration (NOAA) interpolated OLR dataset (Liebmann & Smith, 1996), which has a spatial resolution of 2.5 degrees latitude \times 2.5 degrees longitude. To quantify the relationships between the jet indices and several teleconnection patterns, we make use of monthly indices of the NAO (North Atlantic Oscillation) and PNA (Pacific-North America pattern) from the National Weather Service Climate Prediction Center, and we use the monthly Niño 3.4 index (i.e., sea surface temperatures averaged over 5°N–5°S, 170°W–120°W) to represent ENSO (El Niño–Southern Oscillation). Our observational analysis is based on the 40-year period from January 1979 to December 2018, over which time we assume that there are 120 independent samples (3 months each for 40 years).

To compare the observed jet variability with that in global climate models, we examine output from the historical runs of 23 global climate models that participated in phase 6 of the Coupled Model Intercomparison Project (CMIP6; Eyring et al., 2016), which are listed in Table S1 in the supplementary material. The historical runs of the models are designed to simulate the past climate over the period 1850–2014 by prescribing observed changes in radiative forcings (greenhouse gases, stratospheric and tropospheric ozone, tropospheric aerosols, volcanic

eruptions, changes in solar output, etc.). We examine one ensemble member per model. The spatial resolution of the model output is highly variable and ranges from about 0.7 degrees to about 2.8 degrees (Table S1), so before analysis, all variables are interpolated to a common spatial resolution of 2.5 degrees latitude \times 2.5 degrees longitude. All of the model analyses are based on the 36-year period from 1979 to 2014, as the models' historical runs end in 2014. The observational analysis based on the 40-year period from 1979 to 2018 is very similar to that based on the 36-year period from 1979 to 2014 and thus can be directly compared to the model analyses in this study.

2.2 Methods

To define the position and strength of the PFJ and STJ, we exploit the fact that the STJ is defined by a baroclinic vertical structure (strong westerlies aloft and near-zero surface winds), whereas the PFJ is defined by an equivalent barotropic vertical structure (westerly wind maximum throughout the depth of the vertical column). Even though the wind speeds associated with both jets are maximized in the upper troposphere, it is challenging to uniquely identify the position and strength of each jet using the upper tropospheric wind field alone. Thus, following previous studies, we define the position and strength of the PFJ using the lower tropospheric wind field (e.g., Ceppi & Hartmann, 2013; Barnes & Polvani 2013). Specifically, in this study, we define the position of the PFJ as the latitude of the maximum of the lower tropospheric (850 hPa) zonal wind averaged over a given longitude band between 20°N and 65°N. The location of maximum winds is determined by fitting a quadratic to the peak and finding the latitude of maximum wind speed at an interval of 0.01° (Barnes & Polvani, 2013). The strength of the PFJ is then determined using the value of the 850 hPa zonal wind at the identified PFJ latitude.

We define the position of the STJ as the latitude of the maximum value found in the difference field between the upper tropospheric (250 hPa) zonal wind and the lower tropospheric (850 hPa) zonal wind averaged over a given longitude band between 10°N and 40°N. The lower tropospheric zonal wind is subtracted to isolate the vertically integrated thermal wind shear (Davis & Birner, 2016), as the STJ is defined by strong westerlies aloft and near-zero surface winds. In the zonal mean, this method yields a comparable position to the NH subtropical jet identified using tropopause height gradients (Maher et al., 2020). The strength of the STJ is then determined using the value of the upper tropospheric (250 hPa) zonal wind at the identified STJ latitude. Note that, in contrast to Menzel et al. (2019), we define the STJ strength index using only the 250hPa zonal wind instead of the difference between 250hPa and 850hPa zonal wind. We choose this definition because the subtropical jet is by definition located in the upper troposphere, and these two definitions yield very similar STJ strength indices ($r = 0.9132$).

The above definitions of the jet streams have been used in a number of recent studies for zonal-mean diagnostics (Adam et al. 2018; Waugh et al. 2018). However, here we intend to apply these definitions both in the zonal mean and at specific longitudes. To do this, we define regional jet indices, in which north-south zonal wind profiles are averaged over specific longitude bands prior to finding the jet positions and strengths. The six regions are defined as: Europe (0°-50°E), Asia (50°E-130°E), the Western Pacific Ocean (130°E-160°W), the Eastern Pacific Ocean (160°W-130°W), North America (130°W-80°W), and the Atlantic Ocean (80°W-0°). We also calculate the four jet indices (PFJ position, PFJ strength, STJ position, STJ strength) at each individual longitude (i.e., using the north-south zonal wind profile at each longitude) (see Fig. 1).

3. Observed variability in the subtropical and polar front jet streams

We begin by reviewing the observed climatology of the NH wintertime jet positions and strengths. Figure 1 shows the NH wintertime (December–February) climatological positions (Fig. 1a) and strengths (Fig. 1b and Fig. 1c) of the polar front and subtropical jets along with their standard deviations at each longitude. In the NH wintertime climatology, there are clearly two distinct jets in Eurasia, the Eastern Pacific Ocean, and the North Atlantic Ocean, while the STJ and PFJ are merged into a single jet stream in East Asia, the Western Pacific Ocean, and the Eastern United States (Fig. 1a), as also documented in previous studies (Christenson et al., 2017; Eichelberger & Hartmann, 2007; Koch et al., 2006; C. Li & Wettstein, 2012). The PFJ position has a similar standard deviation at most longitudes (6.73 degrees latitude on average), with the largest standard deviations occurring over western Eurasia. In contrast, the standard deviation of the STJ position varies more substantially by longitude, with very small standard deviations (2.09 degrees latitude) over Eurasia and the western Pacific Ocean and standard deviations comparable to that of the PFJ position at most other longitudes.

The strength of the two jets also varies by region. The strength of the PFJ (as measured by the 850-hPa zonal wind maximum) is largest (10–15 m/s zonal wind at 850 hPa) and displays the most variance over the storm track regions of the North Pacific and North Atlantic Oceans (Fig. 1b). The strength of the STJ (as measured by the 250-hPa zonal wind maximum) is largest (> 40 m/s zonal wind at 250 hPa) over Eurasia and the western Pacific Ocean, with the largest wind speeds (~70 m/s) observed where the STJ and PFJ are merged over the western Pacific Ocean (Fig. 1c). A secondary peak in STJ strength is also observed in eastern North America where the two jets are merged. The standard deviation of the STJ strength varies little with longitude.

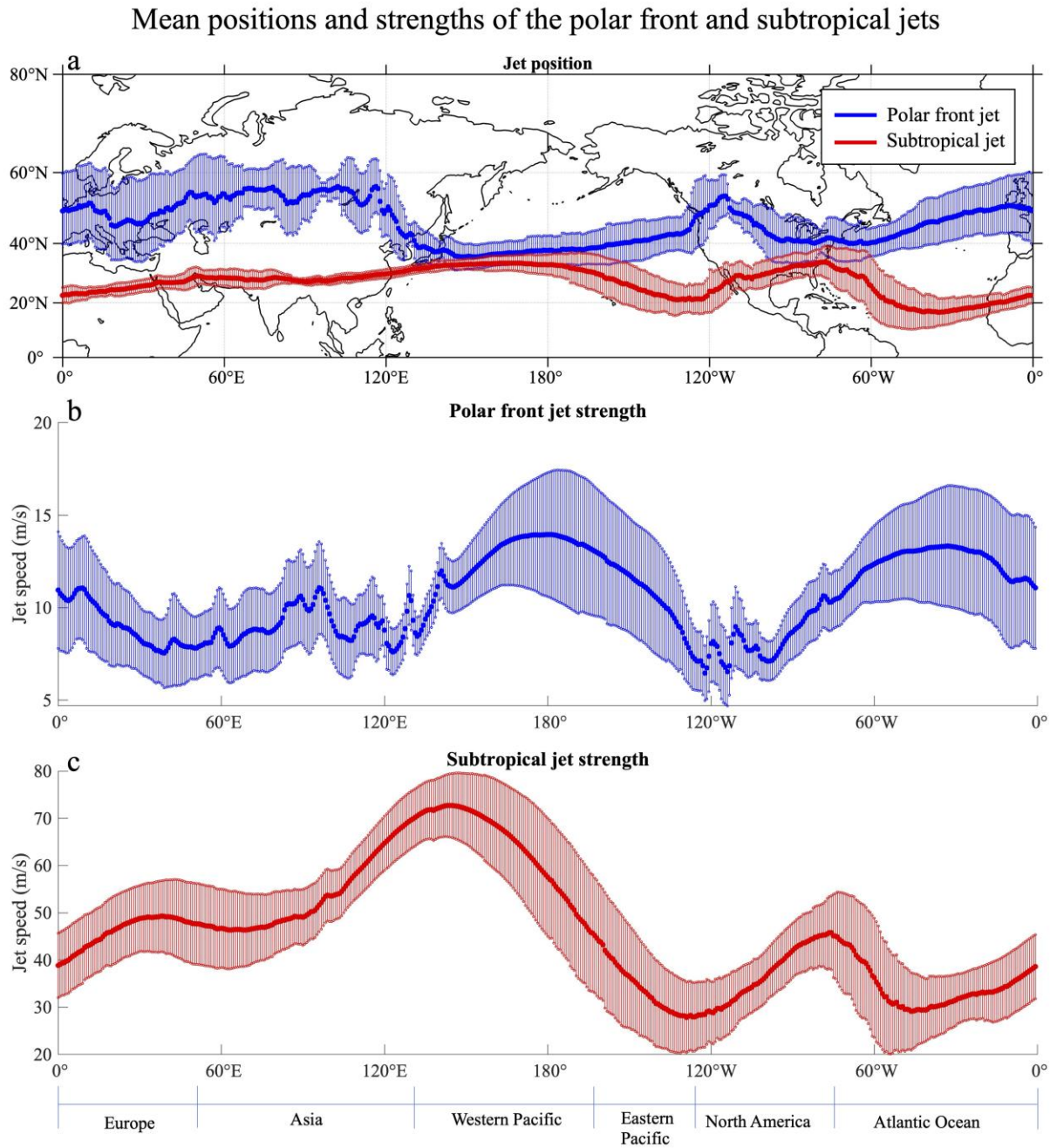


Figure 1. Mean positions (a) and strengths (b and c) of NH wintertime (December–February) polar front and subtropical jet with ± 1 standard deviation (shading) shown at all longitudes using jet indices derived from the ERA-Interim reanalysis dataset from 1979–2018. Note that the jet speeds in panels b and c are plotted on different scales. The polar front jet is defined at 850 hPa, whereas the subtropical jet is defined at 250 hPa.

We next examine whether variability in the jet strengths and positions are correlated with one another, as could be anticipated from the results of Lee and Kim (2003). Figure 2 shows the correlations among the monthly time series of the positions and strengths of the STJ and PFJ. The correlations are shown for the zonal-mean (leftmost bar in each panel) and the six different regions defined in Section 2.2. The horizontal dashed lines in each panel indicate the minimum value for statistically significant correlations at the 95% confidence level.

With respect to the overall correlations between position and strength from the zonal-mean wind field, few statistically significant correlations are found, consistent with the results of Menzel et al. (2019). A significant negative correlation is found between the PFJ position and STJ strength (Fig. 2b), as a more poleward distinct PFJ is associated with a weaker STJ (as could be anticipated from the results of Lee and Kim 2003). A weakly significant positive correlation is also found between the strength and position of the STJ (Fig. 2d), in contrast to the weak negative correlation found in climate models by Menzel et al. (2019). This difference is due to the fact that Menzel et al. (2019) defined STJ strength using the difference field between the upper tropospheric (250 hPa) zonal wind and the lower tropospheric (850 hPa) zonal wind, whereas in this study, we use only the upper tropospheric (250 hPa) zonal wind to define the STJ strength. If we define the STJ strength as in Menzel et al. (2019), we also find a weak negative correlation (-0.0718) between STJ position and strength.

However, the weak correlations among the positions and strengths of the jets in the zonal mean mask significant correlations among the positions and strengths of the jets that occur on the regional level, which highlights the need to examine the variability of the jets and the underlying mechanisms at individual longitudes. As in the zonal mean (Davis & Birner 2017; Waugh et al.,

2018; Menzel et al., 2019), there are few significant correlations between the positions of the PFJ and STJ, except in the Eastern Pacific and Atlantic sectors where a small negative relationship is observed (Fig. 2a). Consistent with the results of Lee and Kim (2003), the PFJ position is negatively correlated with the STJ strength in the zonal mean, and this negative correlation arises predominantly from the Pacific Ocean regions (Fig. 2b). However, in other regions, the correlations are small. The strength and position of the PFJ are positively correlated over continents and negatively correlated over oceans (Fig. 2c), whereas the strength and position of the STJ are positively correlated in all regions (Fig. 2d). Significant positive correlations also exist between the PFJ strength and STJ position/strength over the Pacific Ocean, particularly in the Western Pacific where there is a merged jet (Fig. 2e and Fig. 2f). We note that Gillett et al. (2021) recently documented significant negative correlations between SH PFJ position and STJ position in Indo-Pacific regions (consistent with the sign of the correlations in the eastern North Pacific and North Atlantic Oceans in Fig. 2a), but significant negative correlations between SH PFJ strength and STJ strength in Indo-Pacific regions (in contrast to Fig. 2f).

Cross-correlations between four jet indices

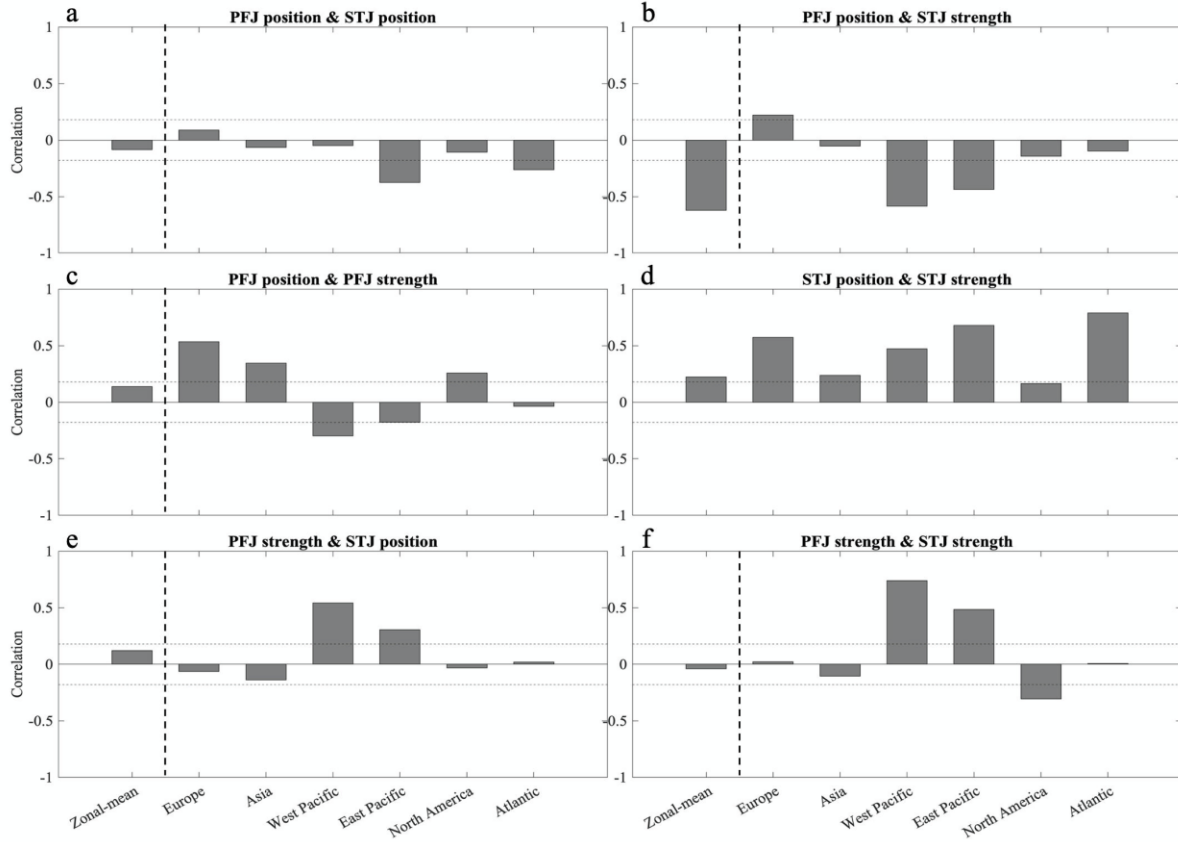


Figure 2. Correlations between monthly time series of the positions and strengths of the subtropical and polar front jets during NH winter, based on ERA-Interim reanalysis (1979–2018). The jets are defined in the zonal mean and for the six different regions defined in Section 2.2. The seasonal cycle is removed prior to the analysis. The horizontal dashed lines in each panel indicate the minimum value for significant correlations at the 95% confidence level according to a two-tailed Student’s t-test.

To interpret the correlations shown in Fig. 2, we now examine the spatial patterns of surface temperature and OLR anomalies associated with variability in the positions and strengths of the jets. To do this, we regress monthly anomalies of OLR and surface temperature onto each of our four jet indices (PFJ position, PFJ strength, STJ position, STJ strength) for NH winter

275 months (i.e., the jet indices are 120 months for the 40-year ERA-Interim reanalysis record).
276 Before the regression analysis, we remove the seasonal cycle of each timeseries by subtracting
277 the monthly-mean values from each month and normalize the jet indices by subtracting the mean
278 and then dividing by the standard deviation. Results for the PFJ and STJ are shown in the
279 following two subsections. We note that, in general, regressions on the distance between the two
280 jets (i.e., the difference in the PFJ and STJ latitudes) (not shown) closely resemble those
281 associated with the PFJ position, which has a greater standard deviation at most longitudes (Fig.
282 1a). Only over the eastern Pacific Ocean and Atlantic Ocean do regressions on the distance
283 between the two jets also resemble those associated with the STJ position, suggesting that both
284 the PFJ and STJ position play comparable roles in affecting the separation distance between the
285 jets at these longitudes.

3.1 Polar front jet

Regression of surface temperature onto polar front jet position (observed)

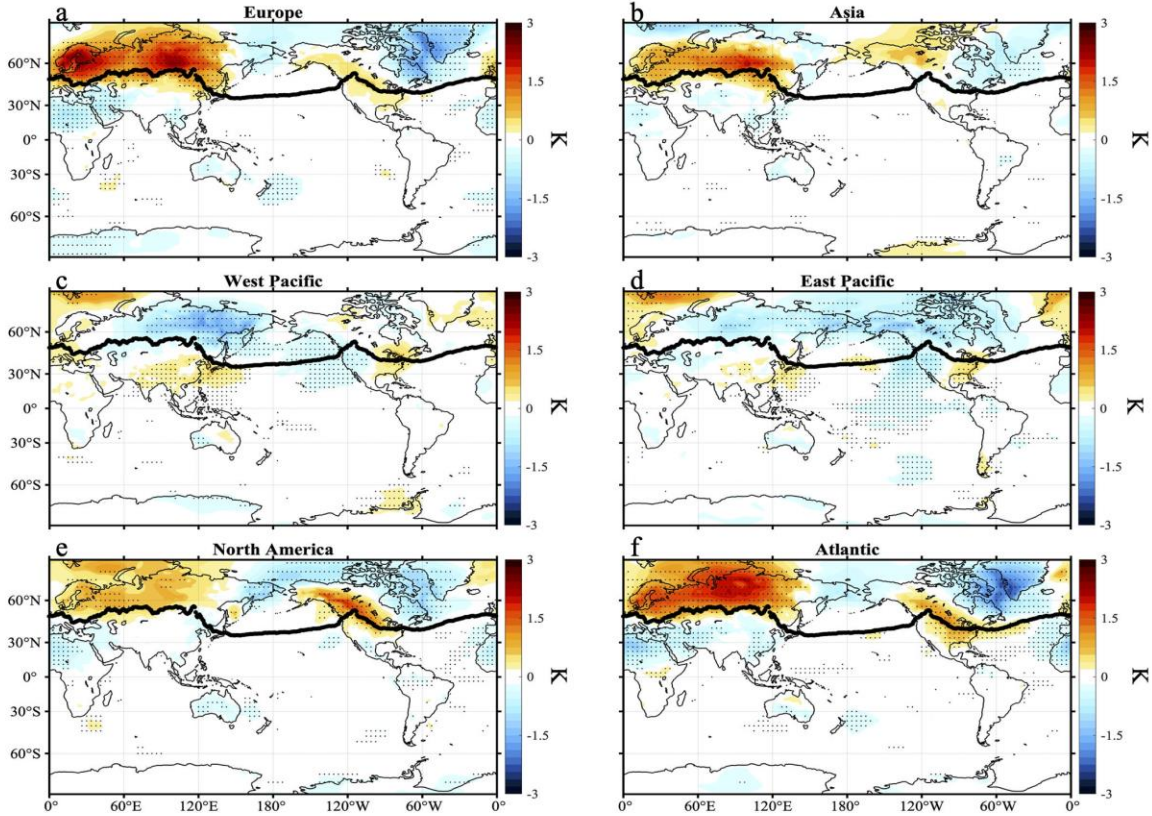


Figure 3. Regression of wintertime monthly surface temperature anomalies onto six different regions' PFJ position in observations. Patterns correspond to surface temperature anomalies associated with a one standard deviation poleward shift of the polar front jet in each region. Thick black lines on each panel are climatological PFJ positions in observations as shown in Fig. 1a. Stippling indicates that regression patterns are statistically significant at the 95% level according to a two-tailed Student's t-test. The model version of this figure is shown in Fig. S1 in the supplementary material.

Figure 3 shows the regressions of observed wintertime surface temperature anomalies

onto the position of the PFJ in six regional sectors (as defined in Section 2.2). The surface
 temperature anomalies shown in each panel correspond to a one standard deviation poleward
 shift of the PFJ in each of the six regional sectors. Based on idealized aqua-planet simulations,
 we expect the location of the polar front jet to be controlled closely by shifts in local
 baroclinicity (Brayshaw et al., 2008). Consistent with this expectation, we see a close
 correspondence in Fig. 3 between surface temperature anomalies and the PFJ position in all
 regional sectors except the eastern Pacific. Regressions of anomalies in the surface meridional
 temperature gradient onto the position of the PFJ confirm that a poleward shift of the PFJ in
 these regions is associated with an increase in the local meridional temperature gradient to the
 north of the PFJ (see Fig. S2). In Europe and Asia, the climatological PFJ position is between
 45°N and 55°N (Fig. 1), so an anomalously warm Eurasian continent is correlated with a shift in
 the maximum baroclinicity further poleward, which is consistent with a poleward European and
 Asian PFJ shift (Figs. 3a-b). Likewise, in North America, the climatological PFJ position is
 oriented from northwest-to-southeast to the east of the Rocky Mountains (Fig. 1a), so anomalous
 warming over the interior of the North American continent and anomalous cooling near the
 Labrador Sea is linked with a shift of the maximum baroclinicity and North American PFJ
 further poleward (Fig. 3e). Alternatively, because the West Pacific PFJ is located at around
 40°N to the south of eastern Russia (Fig. 1a), anomalous cooling over the continent to the north
 is consistent with a shift in the maximum baroclinicity and West Pacific PFJ further poleward
 (Fig. 3c). Similarly, anomalous cooling over the Labrador Sea and Greenland is associated with
 a poleward shift of the baroclinicity and PFJ over the Atlantic sector (Fig. 3f).

The PFJ position is also closely linked to well-known global teleconnection patterns. For
 example, the surface temperature anomalies associated with poleward shifts in the PFJ in the

Atlantic, European, and North American sectors closely resemble those associated with the positive phase of the NAO, which is characterized by above-normal temperatures over northern Europe and below-normal temperatures over Greenland and Eastern Canada (Hurrell, 1995). In the eastern Pacific sector, the surface temperature anomalies associated with a poleward shift in the PFJ closely resemble those associated with the negative phase of the PNA (Wallace & Gutzler, 1981; Yu & Lin, 2019) and the cool phase of ENSO (Halpert & Ropelewski, 1992; Ropelewski & Halpert, 1989). A more detailed discussion about the linkages to the teleconnection patterns is provided below in Section 3.3.

Regression of surface temperature onto polar front jet strength (observed)

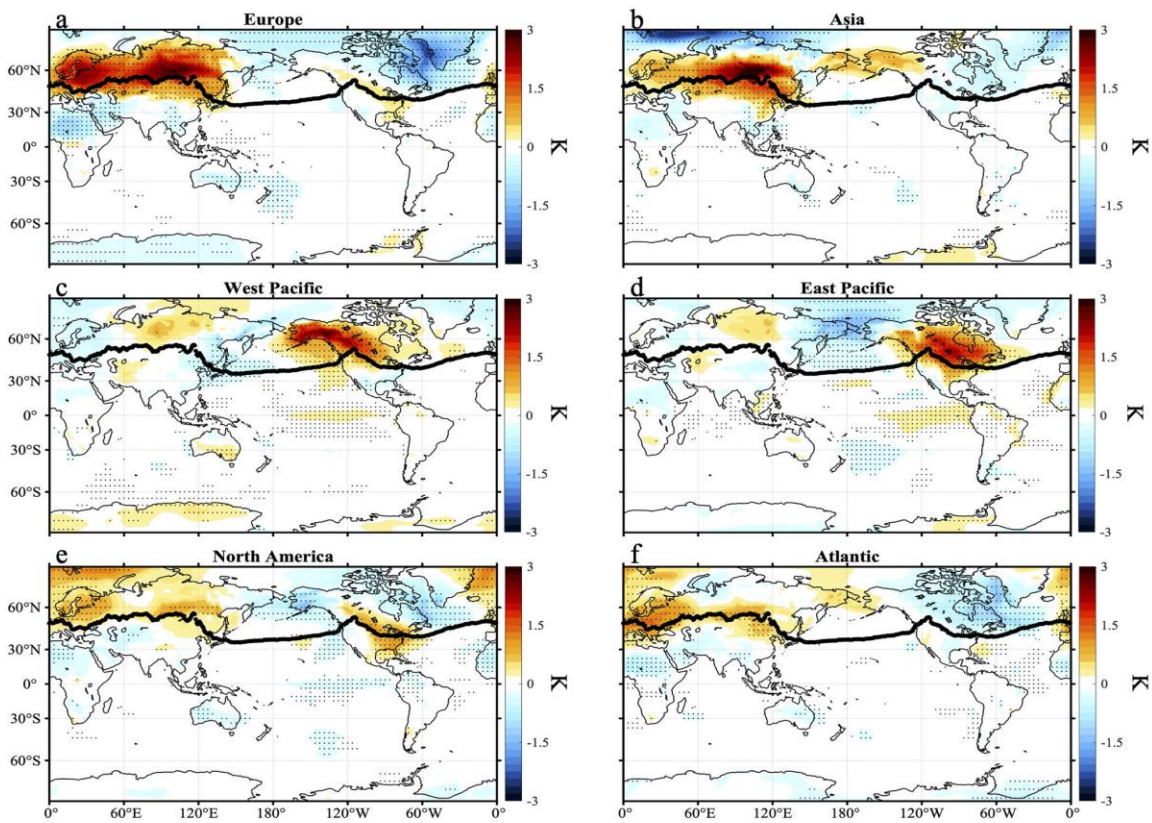


Figure 4. As in Fig. 3, but for the PFJ strength. The model version of this figure is shown in Fig. S3 in the supplementary material.

Figure 4 shows analogous results to Fig. 3, but for the PFJ strength. For reference, regressions of anomalies in surface meridional temperature gradient on PFJ strength are shown in Fig. S4. The regression patterns of surface temperature anomalies onto PFJ strength (Fig. 4) are similar to that of PFJ position (Fig. 3) for Europe, Asia, and North America, but very different in the Pacific. This suggests that similar processes are associated with variations in PFJ position and intensity over the continents, but not necessarily over the oceans (see also Fig. 2c). As for the PFJ strength in the Pacific sector, the surface temperature anomalies associated with PFJ intensification closely resemble those associated with the positive phase of PNA and the warm phase of the ENSO (Wallace & Gutzler, 1981; Yu & Lin, 2019; Halpert & Ropelewski, 1992; Ropelewski & Halpert, 1989). Intensification of the western and eastern Pacific PFJ is associated with enhanced convection (anomalously low OLR) in the eastern tropical Pacific Ocean and suppressed convection (anomalously high OLR) in the western tropical Pacific Ocean (Fig. S5). Alternatively, intensification of the North American PFJ is associated with the cool (La Niña) phase of ENSO (Fig. S5). Intensification of the PFJ in other regions is not associated with significant variations in tropical convection (Fig. S5), and variability in tropical convection also has little to no correlation with variability in PFJ position in any region except the eastern Pacific.

We note that the regression maps of surface temperature anomalies on the zonal-mean PFJ position closely resemble those of the Europe, Asia, North America, and Atlantic sectors (compare Fig. S6a to Fig. 3), whereas the regression maps of surface temperature anomalies on the zonal-mean PFJ strength closely resemble those of the western and eastern Pacific Ocean sectors (compare Fig. S6b to Fig. 4). This is because the zonal-mean PFJ strength is dominated by the PFJ in Pacific where it is strongest (Fig. 1b).

3.2 Subtropical jet

Figures 5 and 6 show the regressions of observed wintertime OLR anomalies onto the position and strength of the STJ in six regional sectors (as defined in Section 2.2). The OLR anomalies shown in each panel correspond to a one standard deviation poleward shift (Fig. 5) or strengthening (Fig. 6) of the STJ in each of the six regional sectors. We also examined regressions of wintertime surface temperature anomalies onto the position and strength of the STJ (Figs. S7 and S8), which highlighted relationships with well-known teleconnection patterns. We will discuss these linkages in Section 3.3.

Previous studies have concluded that tropical convection plays a critical role in forcing the position and strength of the STJ locally, particularly over the Pacific sector where El Niño is known to strongly modify the subtropical jet (Gallego et al., 2005; Lu et al., 2008; Seager et al., 2003). Over the western Pacific, enhanced convection is associated with a strengthening and poleward shift of the STJ (Figs. 5c and 6c), consistent with the idealized model results of Lee and Kim (2003) and Son and Lee (2005) and the correlation between western Pacific STJ latitude and speed in Fig. 2d. Over the eastern Pacific, there is a robust relationship between enhanced convection (an El Niño-like pattern) and a strengthened STJ, but there is only a weak relationship between local convection and the STJ position (Figs. 5d and 6d). Additionally, there is a robust relationship between a strengthened STJ over Asia and enhanced convection over the same longitude band (i.e., over the northern Indian Ocean). We note that the regression map of OLR anomalies on the zonal-mean STJ strength closely resembles that of the eastern Pacific Ocean sector (compare Fig. S6d to Fig. 6d).

At most other longitudes, the variability in the STJ latitude and strength is more strongly linked to teleconnections from remote tropical convection anomalies over the Pacific basin than

to tropical convection anomalies at the same longitude. We note that these relationships also exist when the tropical Pacific convection anomalies lead the variability in the STJ latitude and strength by one month (not shown). Figure 5 shows that a poleward shift of the STJ over Europe, Asia, and North America is associated with enhanced convection over western tropical Pacific Ocean (i.e., a La Niña-like pattern). A similar pattern of OLR anomalies is also found for regressions on the zonal-mean STJ position (Fig. S6c). The large influence of ENSO on the position of the North American STJ is consistent with the well-known teleconnections of ENSO over North America (Cook & Schaefer, 2008; Eichler & Higgins, 2006; Ropelewski & Halpert, 1989; Smith, Green, Leonardi, & O'Brien, 1998). As for the STJ strength, Figure 6 shows that enhanced convection in the eastern tropical Pacific Ocean (i.e., an El Niño-like pattern) is associated with a strengthened STJ over North America. Because enhanced convection in the western tropical Pacific Ocean is associated with a strengthened PFJ over North America (Fig. S5), there is a negative correlation between PFJ and STJ strength over North America (Fig. 2f).

To summarize these relationships, the left column of Figure 7 shows the regression coefficients of observed tropical (5°N - 5°S) OLR anomalies onto indices of the STJ position and strength calculated at every longitude (as shown for the climatology in Fig. 1). In other words, for each longitude on the y-axis in Fig. 7, the horizontal line at that y-value shows the zonal cross section of tropical OLR anomalies associated with STJ variability at that longitude. Figure 7 reveals that the STJ variability at nearly all longitudes is associated with a dipole of OLR anomalies over the tropical Pacific Basin. This figure shows the dominance of ENSO (rather than local tropical convection) in governing STJ variability globally.

Consistent with Fig. 5, Fig. 7a reveals that a La Niña-like pattern of anomalous tropical convection is associated with a poleward shift of the subtropical jet from the eastern Atlantic

Ocean to the east coast of Asia, and over North America. Consistent with Fig. 6, Fig. 7c reveals that enhanced tropical convection from the western Indian Ocean to the eastern Pacific Ocean strengthens the STJ at that longitude. Looking across all longitudes, a La Niña-like pattern of anomalous tropical convection strengthens the STJ over the eastern Atlantic Ocean, western Europe, and the western Pacific Ocean, and an El Niño-like pattern of anomalous tropical convection strengthens the STJ over the eastern Pacific Ocean and North America (Seager et al., 2003).

Regression of OLR onto subtropical jet position (observed)

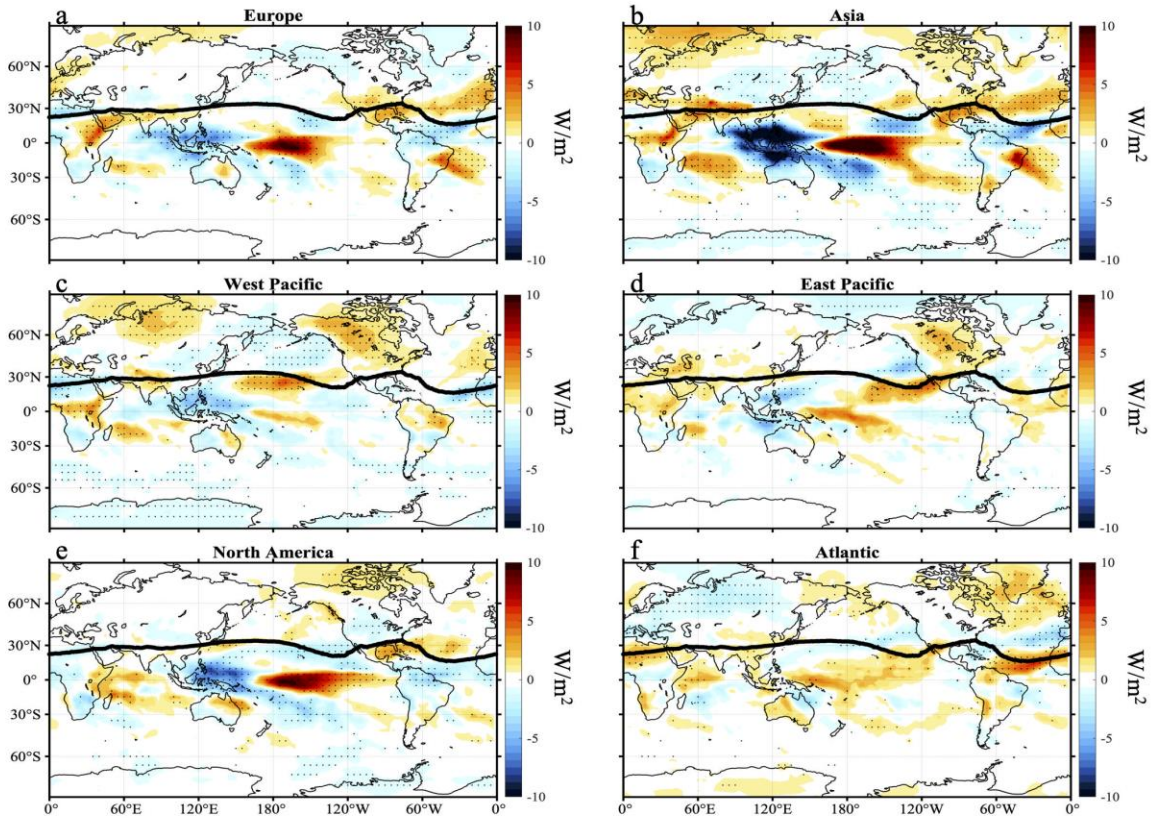


Figure 5. Regression of wintertime monthly OLR anomalies onto six different regions' subtropical jet position in observations. Patterns correspond to OLR anomalies associated with a one standard deviation of poleward shift of the subtropical jet in each region. Thick black lines on each panel are climatological STJ positions in observations as shown in Fig. 1a. Stippling

indicates that regression patterns are statistically significant at the 95% level according to a two-tailed Student's t-test. The model version of this figure is shown in Fig. S9 in the supplementary material.

Regression of OLR onto subtropical jet strength (observed)

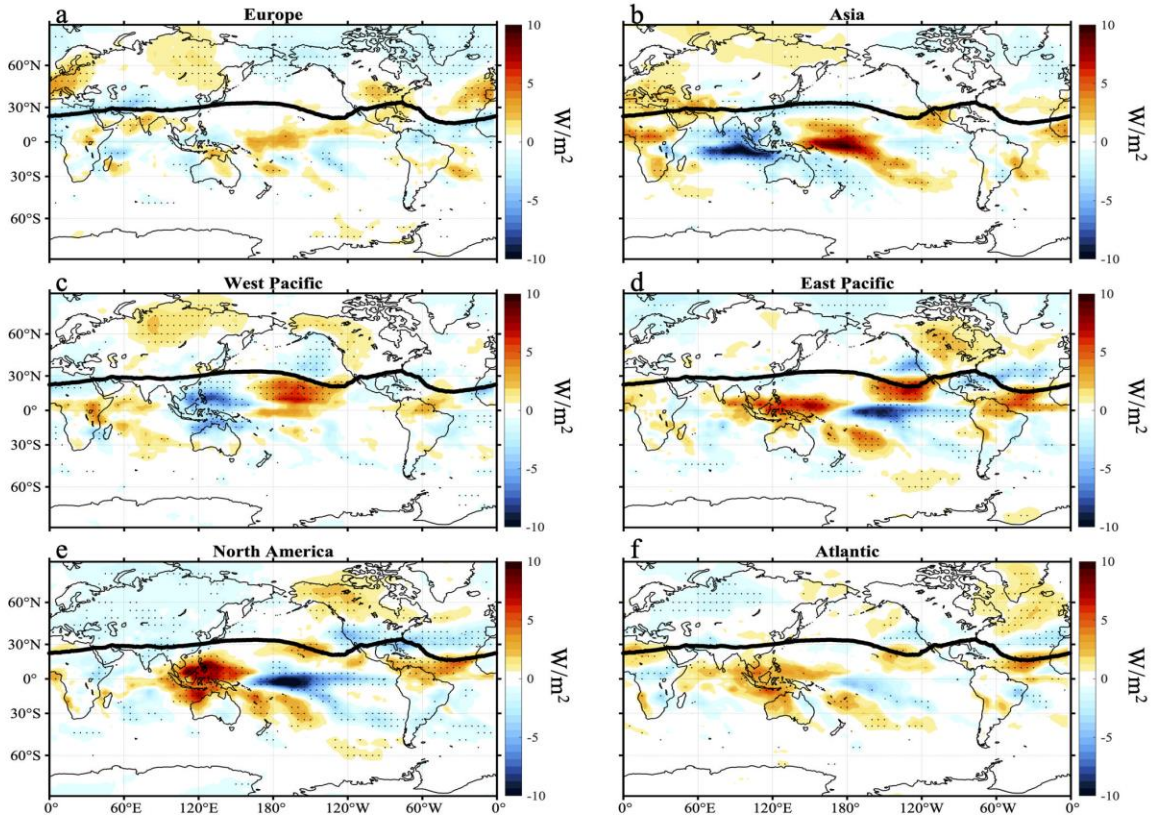


Figure 6. As in Fig. 5, but for STJ strength. The model version of this figure is shown in Fig. S10 in the supplementary material.

3.3 Correlations of jet indices with teleconnection patterns

To summarize the linkages between jet variability and teleconnection patterns, Tables 1 and 2 show the correlations between the wintertime monthly time series of three teleconnection patterns (NAO, PNA, and ENSO) and the wintertime monthly time series of the positions and

intensities of the jets in each of the six regions, as well as the zonal mean. Table 1 shows the correlations between the teleconnection indices and the PFJ position/strength, and Table 2 shows the same correlations but for the STJ position and strength.

As shown in Table 1, consistent with Figs. 3-4, the positive phase of the NAO is significantly correlated with a poleward shift and a strengthening of the PFJ in the Europe, North America, and Atlantic sectors (Strong & Davis, 2008; Woollings et al., 2010). The positive phases of the PNA and ENSO are significantly correlated with an equatorward shift and strengthening of the PFJ in the Pacific Ocean and a weakening of the PFJ over North America (see also Fig. S5).

For the STJ position and strength (Table 2), the positive phase of the NAO is significantly correlated with a poleward shift and a strengthening of the STJ in Eurasia and an equatorward shift and a weakening of the STJ in the Atlantic. The positive phase of the NAO is also associated with a weakening of the STJ in the eastern Pacific and North America. These results are consistent with previous studies, which showed that the positive phase of the NAO is associated with separated jets in the Atlantic sector (Ambaum et al., 2001; Yuan et al., 2011) and a weakening of the STJ in the Pacific sector (Ambaum et al., 2001). The positive phase of the PNA is significantly correlated with a poleward shift and a strengthening of the STJ in the Pacific Ocean, particularly in the western Pacific (Strong & Davis, 2007), and an equatorward shift of the STJ in North America (Rodionov & Assel, 2001). Consistent with Figs. 5 and 7a, La Niña (negative phase of ENSO) is associated with a poleward shift of STJ in Europe, Asia, and North America, and consistent with Figs. 6 and 7c, El Niño (positive phase of ENSO) is associated with a strengthened STJ over the eastern Pacific Ocean and North America.

The correlations between the teleconnection indices and the zonal-mean jets generally

mirror the behavior of the jets in the longitude bands with the largest correlations (see also Fig. S6). One exception is the relationship between NAO and PFJ strength. Even though there are strong correlations between the NAO and PFJ strength in the Europe, North America, and Atlantic sectors, the correlation between the NAO and the zonal-mean PFJ strength is very small. This is because the zonal-mean PFJ strength is dominated by the PFJ in Pacific where it is strongest (Fig. 1b).

Table. 1 Correlations between PFJ indices and teleconnection patterns

	Europe	Asia	West Pacific	East Pacific	North America	Atlantic	Zonal-mean
NAO & PFJ position	0.47	0.14	0.06	0.09	0.31	0.55	0.54
NAO & PFJ strength	0.47	0.07	-0.04	-0.04	0.44	0.43	0.00
PNA & PFJ position	0.12	0.05	-0.33	-0.45	0.16	0.03	-0.34
PNA & PFJ strength	-0.06	0.00	0.78	0.35	-0.26	-0.10	0.27
Niño 3.4 & PFJ position	0.00	-0.01	-0.04	-0.28	0.02	-0.03	-0.15
Niño 3.4 & PFJ strength	0.08	0.06	0.26	0.22	-0.20	0.03	0.22

Table 1. Correlations between NAO index and PFJ position/strength, between PNA index and PFJ position/strength, and between Niño 3.4 index and PFJ position/strength in six regions and zonal-mean during NH winter from 1979 to 2018. Bold numbers are statistically significant correlations at the 95% level according to a two-tailed Student's t-test.

Table. 2 Correlations between STJ indices and teleconnection patterns

	Europe	Asia	West Pacific	East Pacific	North America	Atlantic	Zonal-mean
NAO & STJ position	0.22	0.30	0.19	-0.07	-0.02	-0.48	-0.14
NAO & STJ strength	0.26	0.19	0.01	-0.19	-0.26	-0.39	-0.48
PNA & STJ position	-0.04	-0.07	0.53	0.23	-0.25	0.07	0.26
PNA & STJ strength	0.00	0.01	0.69	0.28	0.10	-0.04	0.50
Niño 3.4 & STJ position	-0.22	-0.41	-0.02	-0.03	-0.34	-0.07	-0.31
Niño 3.4 & STJ strength	-0.06	-0.12	-0.05	0.17	0.31	-0.02	0.25

Table 2. As in Table 1, but for STJ position/strength.

4. Comparison between models and observations

In this section, we compare the observed variability in the position and strength of the jets (as documented in Section 3) with that from CMIP6 models. To do this, we make use of multi-model mean regression maps to summarize the average behavior of CMIP6 models. These maps are calculated as follows. First, the regression maps are calculated individually for each of the 23 CMIP6 models using the wintertime monthly variability of each model over the period 1979–2014 (as shown for the observations in Figs. 3–6). Then, these 23 maps are averaged together to show the multi-model mean pattern of surface temperature and OLR anomalies associated with wintertime jet variability. Note that, if instead we averaged the jet indices and surface temperature and OLR anomalies from each model together before performing the regression, we would average out the internal variability that is the focus of this study.

Model results for the regressions on PFJ position and strength are shown in Figs. S1 and S3, and model results for the regressions on STJ position and strength are shown in Figs. S7 and S8. The model regressions of surface temperature anomalies onto the PFJ position and strength are very similar to those shown for observations (Figs. 3-4), but the model regressions of OLR anomalies onto STJ position and strength differ significantly from observations (Figs. 5-6). For that reason, in this section, we focus on the comparison of the STJ variability between observations and CMIP6 models.

To summarize the model biases in STJ variability, the right column of Fig. 7 shows the CMIP6 multi-model mean regression coefficients of tropical (5°N-5°S) OLR anomalies onto indices of the STJ position and strength calculated at every longitude (as shown in the left column for observations). Consistent with observations (Figs. 5-6), it is worth noting that the

STJ at each longitude in the multi-model mean is not primarily associated with OLR anomalies at its own longitude, but rather is linked to tropical OLR anomalies in the Pacific. However, for the OLR anomalies associated with a poleward shift in the STJ, tropical convection in the models is displaced westward over Eurasia when compared to observations (Figs. 7a-b). Additionally, large discrepancies between the observed and model patterns occur in the North America. Over North America in observations, a La Niña-like pattern in anomalous tropical convection is associated with a poleward shift of the STJ position, but this pattern is not shown in models. For the OLR anomalies associated with a strengthening of the STJ (Figs. 7c-d), most models capture the observed relationship between La Niña and a strengthened STJ over the western Pacific Ocean, and between El Niño and a strengthened STJ over the eastern Pacific Ocean and North America (see the prominent quadrupole pattern in the left-center of panels c and d). However, most models fail to capture the observed relationship between tropical convection and the STJ strength over the eastern Atlantic Ocean and Eurasia.

We now discuss the possible causes of these model-observation discrepancies shown in Fig. 7. As discussed above, models agree that a La Niña-like pattern in anomalous tropical convection is associated with a poleward shift of the STJ position over Eurasia, but the dipole of OLR anomalies is shifted to the west in the multi-model-mean compared to observations (Figs. 7a-b). To illustrate this more clearly, the top row of Fig. 8 shows the regressions of OLR anomalies onto the STJ position in the Asian sector (as shown in Figs. 5 and S7, but zoomed in to show greater detail). In particular, notice that the region of enhanced convection in the multi-model-mean is narrower and confined to longitudes west of the Philippines, and that the region of suppressed convection along the Equator in the multi-model-mean extends much further to the west over New Guinea (Fig. 8b).

One reason for the westward shift of the La Niña-like pattern in models could be that the climatological OLR field in CMIP6 models is different from that in observations, as some previous studies have documented that ENSO diversity is associated with the tropical Pacific background state (Capotondi et al., 2015; Choi, An, Kug, & Yeh, 2011; Chung & Li, 2013). The observed and multi-model-mean OLR climatology in the equatorial Pacific is shown in Fig. 8c and Fig. 8d. The equatorial low OLR region in observations in the western Pacific is wider and extends further eastward than in the multi-model-mean climatology, which is consistent with previous findings that many climate models simulate an excessive westward extension of the cold tongue into the tropical Pacific warm pool (Ding et al., 2020; G. Li & Xie, 2014; Lin, 2007). To illustrate this better, we also plot the cross-section of observed and multi-model-mean climatological OLR at the Equator as a function of longitude in Fig. 8e.

In Fig. 9, we show the correlation between the position of the climatological low OLR region along the Equator in the western Pacific Ocean (as shown in Fig. 8e) and the position of the OLR anomalies associated with a poleward STJ shift over the Asia sector (as shown in Figs. 8a and 8b) across CMIP6 models. The climatological low OLR region is defined as the region where OLR is smaller than 255 W m^{-2} , and we define the position of the low OLR region as the mid-point longitude of the low OLR region in the equatorial western Pacific. The results are not sensitive to the exact choice of threshold value (i.e., values between 250 and 270 W m^{-2} give similar results). The position of the OLR associated with a poleward STJ shift over the Asia sector, which we refer to as the “La Niña pattern index”, is defined as the transition longitude between 120°E - 180°E where the regression coefficient of OLR to Asian STJ position (as shown in Figs. 8a and 8b) averaged over 10° S to 20° N crosses zero. The positive relationship between the midpoint of the climatological low OLR region and the La Niña pattern index ($r = 0.80$)

indicates that the westward La Niña-like pattern in models' tropical convection associated with a poleward STJ shift over the Eurasian sector can be attributed to the biased OLR climatology in the tropical western Pacific Ocean in many models. The western Pacific tropical convection is centered further to the west than observations in nearly all of the models and thus causes a westward shift of the La Niña-like pattern of anomalous tropical convection.

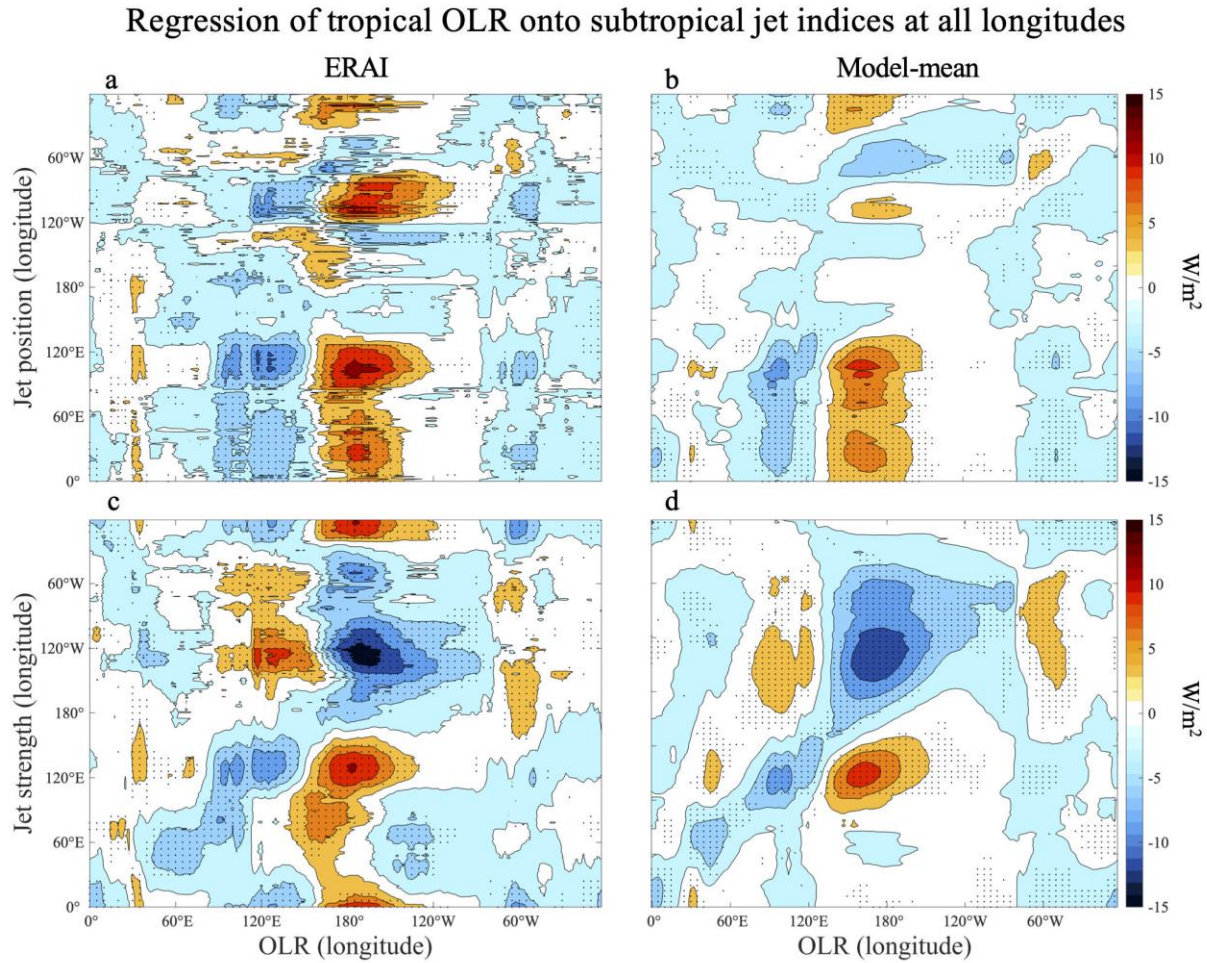


Figure 7. Regression of the wintertime monthly tropical OLR (5°S-5°N) anomalies onto subtropical jet indices at all longitudes. (a) and (b) are regression coefficients for subtropical jet position; (c) and (d) are regression coefficients for subtropical jet strength. The left column shows results for observations, and the right column shows results for the CMIP6 multi-model-mean. Color shading represents the regression coefficient of OLR at the longitude on the x-axis

to the subtropical jet index at the longitude on y axis. For (a) and (c), stippling indicates that regression patterns are statistically significant at the 95% level according to a two-tailed Student's t-test. For (b) and (d), stippling indicates that more than 80% of models agree on the sign of the regression coefficients.

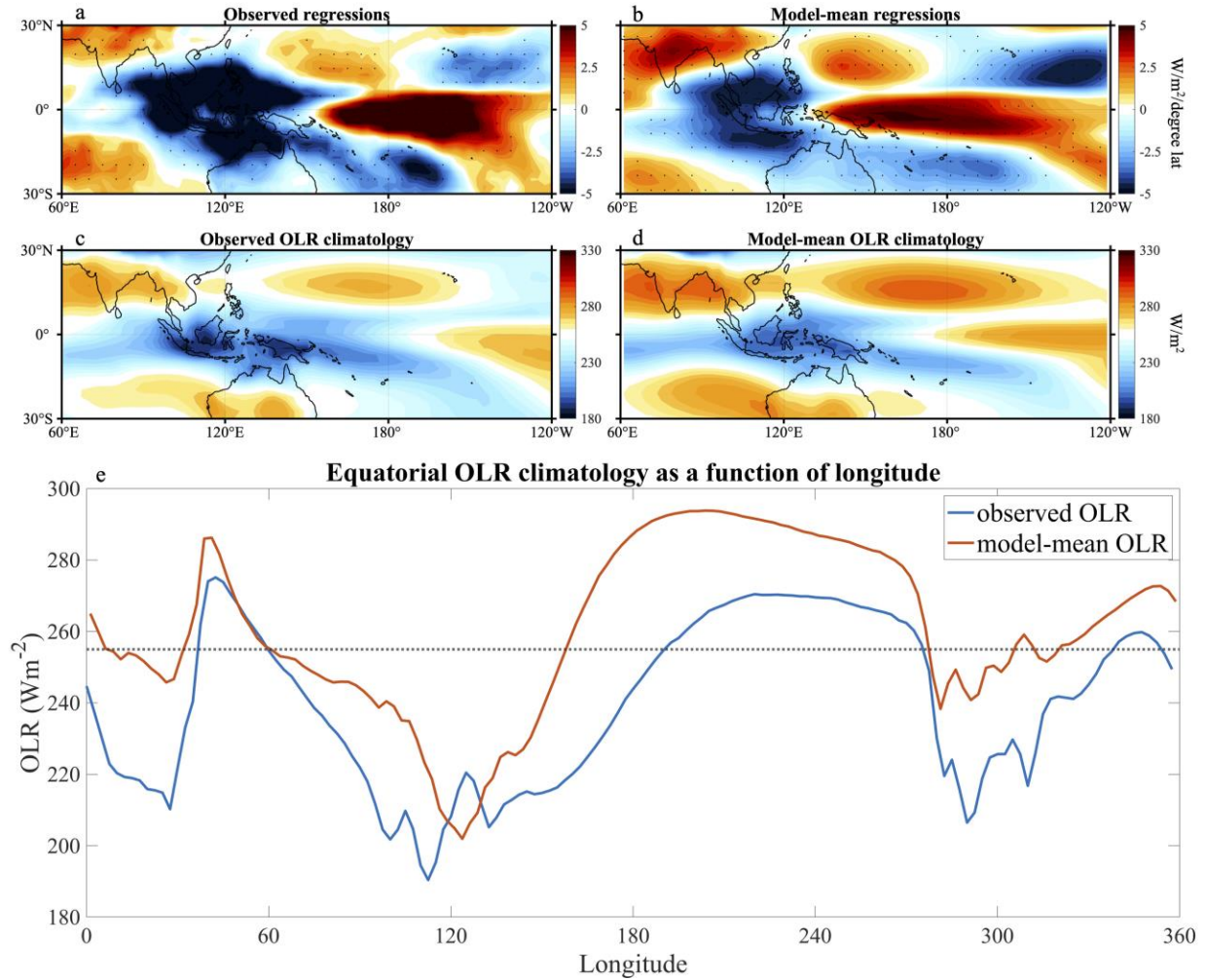


Figure 8. (a) and (b) are regressions of monthly wintertime OLR anomalies to the Asian STJ position for observations and the CMIP6 multi-model mean (reproduced from the second panels of Figure 5 and Figure S7 but zoomed in and with different color scales). (c) and (d) are the wintertime OLR climatology for observations and the CMIP6 multi-model mean. (e) is the observed and multi-model-mean wintertime OLR climatology at the Equator as a function of

longitude. The blue line shows the observed OLR, while the red line shows the model-mean OLR. The dashed black line shows the 255 W m^{-2} OLR value, below which is defined as low OLR.

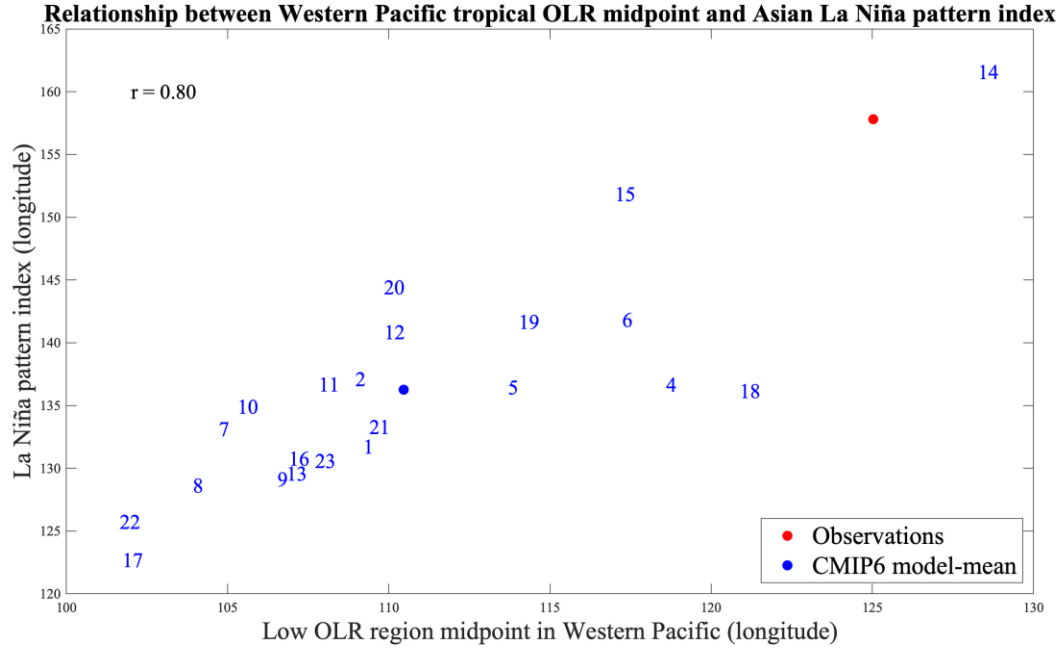


Figure 9. Scatter plot between the midpoint of the wintertime climatological low OLR region over the western Pacific and the La Niña pattern index. The La Niña pattern index is defined as the transition longitude between 120°E - 180°E where the regression coefficient of wintertime monthly OLR anomalies to the Asian STJ position (as shown in Figs. 8a and 8b) averaged over 10°S to 20°N crosses zero. The midpoint of the climatological low OLR region is defined as the mid-point longitude of the low OLR region in equatorial Western Pacific (as shown in Fig. 8e). The low OLR region is defined where the OLR is smaller than 255 W m^{-2} . Numbers on the scatterplot correspond to the models listed in Table S1. The blue dot represents multi-model-mean, while the red dot is for observations.

Another key discrepancy between observations and models shown in Fig. 7 is that models fail to capture the linkage between a La Niña-like pattern of anomalous tropical convection and the poleward shift of the STJ over North America (Fig. 7b). Given the biased OLR climatology in models, it seems plausible that different Rossby wave trains would be excited by tropical convection at different locations associated with El Niño and La Niña patterns in observations and models (Jiménez-Esteve & Domeisen, 2018). To illustrate this, Figure 10 shows the regressions of 500-hPa eddy geopotential height anomalies and anomalies in the 250 hPa – 850 hPa zonal wind difference field (i.e., the field used to calculate the STJ position; see Section 2.2) onto the Niño 3.4 index for both observations and the CMIP6 multi-model mean. Here, the term eddy geopotential height anomalies means that both the zonal mean and seasonal cycle has been removed from the geopotential height data. As shown in Fig. 10a, the wave train excited by anomalous tropical convection in observations is further south and east compared to that in multi-model-mean. Consequently, a north-south dipole of eddy geopotential height anomalies and a north-south dipole of zonal wind anomalies are located directly over the STJ in eastern North America in observations, but not in models.

Finally, we noted above that models fail to capture the observed relationship between a La Niña-like pattern of anomalous tropical convection and STJ strength over the eastern Atlantic and European sectors (Fig. 7d). As shown in Fig. 10a, the wave train associated with ENSO in observations propagates poleward to Alaska and Canada and then back equatorward toward the North Atlantic and Western Europe, where it projects onto the STJ in this region. In the multi-model mean, the wave train associated with ENSO is shifted further westward and thus returns equatorward over the central Atlantic Ocean (Fig. 10b). However, ENSO's impacts in the North Atlantic may be highly variable and unstable (note lack of significance in Fig. 10a and 10b over

North Atlantic), which means that the observed teleconnections in this sector may be highly sensitive to the time frame we choose (Greatbatch, Lu, & Peterson, 2004).

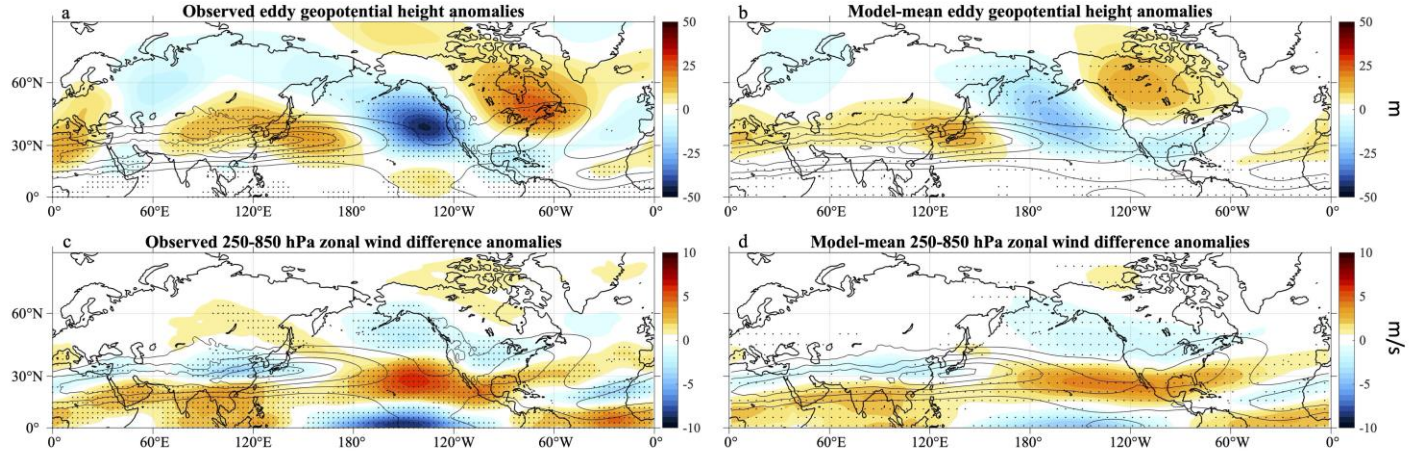


Figure 10. Regression of wintertime monthly eddy 500 hPa geopotential height anomalies (i.e., with both the seasonal cycle and zonal-mean field removed) and 250-850 hPa zonal wind difference anomalies onto the Niño 3.4 index in observations (a, c) and the CMIP6 multi-model mean (b, d). Stippling in (a, c) indicates that regression patterns are statistically significant at the 95% level according to a two-tailed Student's t-test, and stippling in (b, d) indicates that more than 80% of models agree with the sign of regression coefficients. Black contours indicate the climatology of zonal wind difference field (250 hPa zonal wind – 850 hPa zonal wind), which is used to define the STJ position. Contours are shown at 20, 30, 40, 50 and 60 m/s.

5. Summary and conclusions

The position and intensity of the polar front and subtropical jet streams in Northern Hemisphere winter exhibit large spatial and temporal variance. Some previous studies (e.g., Lee & Kim, 2003; Son & Lee, 2005) have provided insight into the processes that control the variability of the polar front and subtropical jets, but most of these studies have relied on

idealized aqua-planet models with no zonal asymmetries in the jets. Although correlations among variations in the strength and position of the jets could be anticipated from such idealized modeling studies, variability in the position and strength of the zonal-mean STJ and PFJ actually exhibit few significant correlations in observations and comprehensive global climate models (Fig. 2; Solomon et al. 2016; Waugh et al. 2018; Menzel et al. 2019; Davis & Birner 2017). The lack of significant correlations among the position and strength of the jets in the zonal-mean mask significant correlations among those of the jets that occur on the regional level (see also Gillett et al. 2021), particularly in the Pacific regions (Fig. 2), which highlights the need to examine the month-to-month and interannual variability of the jets and their possible underlying mechanisms at individual longitudes.

In this study, we find a close relationship between the observed variability in the position and strength of the STJ and tropical outgoing longwave radiation (OLR), and between the observed variability in position and strength of the PFJ with mid-latitude surface temperature gradients during the NH winter season. In many regions, the variability in the positions and strengths of the jets is closely linked to well-known global-scale teleconnection patterns, such as the NAO, PNA, and ENSO (Table 1). Local changes in surface baroclinicity are associated with variability in the position and strength of the NH PFJ at most longitudes outside of the eastern Pacific Ocean (Figs. 3-4). Variations in tropical convection over the Pacific Ocean are linked to variations in the strength and position of the NH STJ at almost all longitudes, with different phases of the El Niño-Southern Oscillation (ENSO) associated with the poleward shift and strengthening of the subtropical jet in different regions (Figs. 5-6).

CMIP6 models generally capture these observed relationships, but for the STJ variability, the models' tropical convection is often displaced westward when compared to observations

(Figs. 7-8). This difference between models and observations can be attributed to the biased OLR climatology over the tropical Western Pacific Ocean in many models, with climatological convection in models displaced westward with respect to observations (Figs. 8-9). The displaced tropical convection in models excites different paths of Rossby wave propagation, making downstream ENSO teleconnections on the STJ over North America, the Atlantic Ocean, and Europe different compared to observations (Fig. 10).

Our study examines observed characteristics of the NH wintertime STJ and PFJ at all longitudes and provides insight into the processes governing their month-to-month and interannual variability over the last four decades. Future work could extend this study to the Southern Hemisphere (expanding the results of Gillett et al. 2021 to all longitudes), or investigate the jet variability in other seasons in the NH. It may also be worthwhile to examine whether the relationships documented here change in the future as the climate warms. Although climate models show a robust poleward shift of the PFJ in a warming climate (e.g., Barnes & Polvani 2013), the STJ does not show a consistent poleward or equatorward shift, at least in the zonal mean (Davis & Birner 2017; Waugh et al., 2018; Menzel et al., 2019). Recent reanalysis data also show poleward trends in the PFJ latitude (e.g., Allen and Kovilakam 2017; Grise et al. 2018), but inconsistent trends in the STJ latitude (Maher et al., 2020; Manney & Hegglin, 2018). Not only does this suggest that the mechanisms driving the responses of the STJ and PFJ to climate change could be very different (as discussed by Menzel et al. 2019), but it also implies that the character of the general circulation (i.e., preference for a merged jet at some longitudes and two distinct jets at other longitudes) may change as the climate warms, hence modulating month-to-month and interannual variability of the jets and the associated behavior of synoptic weather events.

Acknowledgments

We thank three anonymous reviewers for constructive comments. We acknowledge the World Climate Research Programme, which, through its Working Group on Coupled Modelling, coordinated and promoted CMIP6. We thank the climate modeling groups for producing and making available their model output, the Earth System Grid Federation (ESGF) for archiving the data and providing access, and the multiple funding agencies who support CMIP6 and ESGF. We also thank Carlee Kleppin (University of Virginia) for her initial work on this topic. This material is based in part upon work supported by the National Science Foundation under Grant No. AGS-1752900.

CMIP6 model output is freely available from the Lawrence Livermore National Laboratory (<https://esgf-node.llnl.gov/search/cmip6/>). ERA-Interim reanalysis data are freely available from the European Centre for Medium-Range Weather Forecasts (<https://apps.ecmwf.int/datasets/data/interim-full-moda/>; <https://cds.climate.copernicus.eu/#!/search?text=ERA5&type=dataset>). Monthly outgoing longwave radiation (OLR) datasets are freely available from NOAA Physical Sciences Laboratory (https://psl.noaa.gov/data/gridded/data.interp_OLR.html). Monthly indices of NAO and PNA are freely available from the National Weather Service Climate Prediction Center (https://www.cpc.ncep.noaa.gov/products/MD_index.php).

References

- Adam, O., Grise, K. M., Staten, P., Simpson, I. R., Davis, S. M., Davis, N. A., ... Birner, T. (2018). The TropD software package: Standardized methods for calculating Tropical Width Diagnostics. *Geoscientific Model Development Discussions*, 1–35. <https://doi.org/10.5194/gmd-2018-124>
- Afargan, H., & Kaspi, Y. (2017). A Midwinter Minimum in North Atlantic Storm Track Intensity in Years of a Strong Jet. *Geophysical Research Letters*, 44(24), 12,511–12,518. <https://doi.org/10.1002/2017GL075136>
- Allen, R. J., & Kovilakam, M. (2017). The role of natural climate variability in recent tropical expansion. *Journal of Climate*, 30(16), 6329–6350. <https://doi.org/10.1175/JCLI-D-16-0735.1>
- Ambaum, M. H. P., Hoskins, B. J., & Stephenson, D. B. (2001). Arctic Oscillation or North Atlantic Oscillation? *Journal of Climate*, 14(16), 3495–3507. [https://doi.org/10.1175/1520-0442\(2001\)014<3495:AOONAO>2.0.CO;2](https://doi.org/10.1175/1520-0442(2001)014<3495:AOONAO>2.0.CO;2)
- Archer, C. L., & Caldeira, K. (2008). Historical trends in the jet streams. *Geophysical Research Letters*, 35(8), 1–6. <https://doi.org/10.1029/2008GL033614>
- Athanasiadis, P. J., Wallace, J. M., & Wettstein, J. J. (2010). Patterns of wintertime jet stream variability and their relation to the storm tracks. *Journal of the Atmospheric Sciences*, 67(5), 1361–1381. <https://doi.org/10.1175/2009JAS3270.1>
- Bals-Elsholz, T. M., Atallah, E. H., Bosart, L. F., Wasula, T. A., Cempa, M. J., & Lupo, A. R. (2001). The wintertime southern hemisphere split jet: Structure, variability, and evolution. *Journal of Climate*, 14(21), 4191–4215. [https://doi.org/10.1175/1520-0442\(2001\)014<4191:TWSHSJ>2.0.CO;2](https://doi.org/10.1175/1520-0442(2001)014<4191:TWSHSJ>2.0.CO;2)

- 701 Barnes, E. A., & Hartmann, D. L. (2010). Influence of eddy-driven jet latitude on North Atlantic
702 jet persistence and blocking frequency in CMIP3 integrations. *Geophysical Research*
703 *Letters*, 37(23). <https://doi.org/10.1029/2010GL045700>
- 704 Barnes, E. A., & Polvani, L. (2013). Response of the midlatitude jets, and of their variability, to
705 increased greenhouse gases in the CMIP5 models. *Journal of Climate*, 26(18), 7117–7135.
706 <https://doi.org/10.1175/JCLI-D-12-00536.1>
- 707 Brayshaw, D. J., Hoskins, B., & Blackburn, M. (2008). The Storm-Track Response to Idealized
708 SST Perturbations in an Aquaplanet GCM. *Journal of the Atmospheric Sciences*, 65(9),
709 2842–2860. <https://doi.org/10.1175/2008JAS2657.1>
- 710 Capotondi, A., Wittenberg, A. T., Newman, M., Di Lorenzo, E., Yu, J. Y., Braconnot, P., ...
711 Yeh, S. W. (2015). Understanding enso diversity. *Bulletin of the American Meteorological*
712 *Society*, 96(6), 921–938. <https://doi.org/10.1175/BAMS-D-13-00117.1>
- 713 Ceppi, P., & Hartmann, D. L. (2013). On the speed of the eddy-driven jet and the width of the
714 hadley cell in the southern hemisphere. *Journal of Climate*, 26(10), 3450–3465.
715 <https://doi.org/10.1175/JCLI-D-12-00414.1>
- 716 Choi, J., An, S. Il, Kug, J. S., & Yeh, S. W. (2011). The role of mean state on changes in El
717 Niño’s flavor. *Climate Dynamics*, 37(5), 1205–1215. [https://doi.org/10.1007/s00382-010-](https://doi.org/10.1007/s00382-010-0912-1)
718 [0912-1](https://doi.org/10.1007/s00382-010-0912-1)
- 719 Christenson, C. E., Martin, J. E., & Handlos, Z. J. (2017). A synoptic climatology of Northern
720 Hemisphere, cold season polar and subtropical jet superposition events. *Journal of Climate*,
721 30(18), 7231–7246. <https://doi.org/10.1175/JCLI-D-16-0565.1>
- 722 Chung, P. H., & Li, T. (2013). Interdecadal relationship between the mean state and El Niño
723 types. *Journal of Climate*, 26(2), 361–379. <https://doi.org/10.1175/JCLI-D-12-00106.1>

- 724 Cook, A. R., & Schaefer, J. T. (2008). The relation of El Niño-Southern Oscillation (ENSO) to
725 winter tornado outbreaks. *Monthly Weather Review*, 136(8), 3121–3137.
726 <https://doi.org/10.1175/2007MWR2171.1>
- 727 Davis, N., & Birner, T. (2016). Climate model biases in the width of the tropical belt. *Journal of*
728 *Climate*, 29(5), 1935–1954. <https://doi.org/10.1175/JCLI-D-15-0336.1>
- 729 Davis, N., & Birner, T. (2017). On the discrepancies in tropical belt expansion between
730 reanalyses and climate models and among tropical belt width metrics. *Journal of Climate*,
731 30(4), 1211–1231. <https://doi.org/10.1175/JCLI-D-16-0371.1>
- 732 Dee, D. P., Uppala, S. M., Simmons, A. J., Berrisford, P., Poli, P., Kobayashi, S., ... Vitart, F.
733 (2011). The ERA-Interim reanalysis: Configuration and performance of the data
734 assimilation system. *Quarterly Journal of the Royal Meteorological Society*, 137(656), 553–
735 597. <https://doi.org/10.1002/qj.828>
- 736 Dickson, R. R., & Namias, J. (1976). North American Influences on the Circulation and Climate
737 of the North Atlantic Sector. *Monthly Weather Review*, 104(10), 1255–1265.
738 [https://doi.org/10.1175/1520-0493\(1976\)104<1255:NAIOTC>2.0.CO;2](https://doi.org/10.1175/1520-0493(1976)104<1255:NAIOTC>2.0.CO;2)
- 739 Ding, H., Newman, M., Alexander, M. A., & Wittenberg, A. T. (2020). Relating CMIP5 Model
740 Biases to Seasonal Forecast Skill in the Tropical Pacific. *Geophysical Research Letters*,
741 47(5), 1–10. <https://doi.org/10.1029/2019GL086765>
- 742 Eichelberger, S. J., & Hartmann, D. L. (2007). Zonal jet structure and the leading mode of
743 variability. *Journal of Climate*, 20(20), 5149–5163. <https://doi.org/10.1175/JCLI4279.1>
- 744 Eichler, T., & Higgins, W. (2006). Climatology and ENSO-related variability of North American
745 extratropical cyclone activity. *Journal of Climate*, 19(10), 2076–2093.
746 <https://doi.org/10.1175/JCLI3725.1>

- 747 Eyering, V., Bony, S., Meehl, G. A., Senior, C. A., Stevens, B., Stouffer, R. J., & Taylor, K. E.
748 (2016). Overview of the Coupled Model Intercomparison Project Phase 6 (CMIP6)
749 experimental design and organization. *Geoscientific Model Development*, 9(5), 1937–1958.
750 <https://doi.org/10.5194/gmd-9-1937-2016>
- 751 Gallego, D., Ribera, P., Garcia-Herrera, R., Hernandez, E., & Gimeno, L. (2005). A new look for
752 the Southern Hemisphere jet stream. *Climate Dynamics*, 24(6), 607–621.
753 <https://doi.org/10.1007/s00382-005-0006-7>
- 754 Gillett, Z. E., Hendon, H. H., Arblaster, J. M., & Lim, E. P. (2021). Tropical and extratropical
755 influences on the variability of the southern hemisphere wintertime subtropical jet. *Journal*
756 *of Climate*, 34(10), 4009–4022. <https://doi.org/10.1175/JCLI-D-20-0460.1>
- 757 Greatbatch, R. J., Lu, J., & Peterson, K. A. (2004). Nonstationary impact of ENSO on Euro-
758 Atlantic winter climate. *Geophysical Research Letters*, 31(2), 4–7.
759 <https://doi.org/10.1029/2003GL018542>
- 760 Grise, K. M., Davis, S. M., Staten, P. W., & Adam, O. (2018). Regional and seasonal
761 characteristics of the recent expansion of the tropics. *Journal of Climate*, 31(17), 6839–
762 6856. <https://doi.org/10.1175/JCLI-D-18-0060.1>
- 763 Halpert, M. S., & Ropelewski, C. F. (1992). Surface Temperature Patterns Associated with the
764 Southern Oscillation. *Journal of Climate*, 5(6), 577–593. [https://doi.org/10.1175/1520-](https://doi.org/10.1175/1520-0442(1992)005<0577:STPAWT>2.0.CO;2)
765 [0442\(1992\)005<0577:STPAWT>2.0.CO;2](https://doi.org/10.1175/1520-0442(1992)005<0577:STPAWT>2.0.CO;2)
- 766 Handlos, Z. J., & Martin, J. E. (2016). Composite analysis of large-scale environments
767 conducive to western Pacific polar/subtropical jet superposition. *Journal of Climate*, 29(19),
768 7145–7165. <https://doi.org/10.1175/JCLI-D-16-0044.1>

- 769 Held, I. M. (1975). Momentum Transport by Quasi-Geostrophic Eddies. *Journal of the*
770 *Atmospheric Sciences*, 32(7), 1494–1497. [https://doi.org/10.1175/1520-](https://doi.org/10.1175/1520-0469(1975)032<1494:MTBQGE>2.0.CO;2)
771 0469(1975)032<1494:MTBQGE>2.0.CO;2
- 772 Held, I. M., & Hou, A. Y. (1980). Nonlinear Axially Symmetric Circulations in a Nearly Inviscid
773 Atmosphere. *Journal of the Atmospheric Sciences*, 37(3), 515–533.
774 [https://doi.org/10.1175/1520-0469\(1980\)037<0515:NASCIA>2.0.CO;2](https://doi.org/10.1175/1520-0469(1980)037<0515:NASCIA>2.0.CO;2)
- 775 Hurrell, J. W. (1995). Decadal Trends in the North Atlantic Oscillation: Regional Temperatures
776 and Precipitation. *Science*, 269(5224), 676 LP – 679.
777 <https://doi.org/10.1126/science.269.5224.676>
- 778 Jiménez-Esteve, B., & Domeisen, D. I. V. (2018). The tropospheric pathway of the ENSO-North
779 Atlantic teleconnection. *Journal of Climate*, 31(11), 4563–4584.
780 <https://doi.org/10.1175/JCLI-D-17-0716.1>
- 781 Kaas, E., & Branstator, G. (1993). The Relationship between a Zonal Index and Blocking
782 Activity. *Journal of Atmospheric Sciences*, 50(18), 3061–3077.
783 [https://doi.org/10.1175/1520-0469\(1993\)050<3061:TRBAZI>2.0.CO;2](https://doi.org/10.1175/1520-0469(1993)050<3061:TRBAZI>2.0.CO;2)
- 784 Kim, H. K., & Lee, S. (2004). The wave-zonal mean flow interaction in the Southern
785 Hemisphere. *Journal of the Atmospheric Sciences*, 61(9), 1055–1067.
786 [https://doi.org/10.1175/1520-0469\(2004\)061<1055:TWMFII>2.0.CO;2](https://doi.org/10.1175/1520-0469(2004)061<1055:TWMFII>2.0.CO;2)
- 787 Koch, P., Wernli, H., & Davies, H. C. (2006). An event-based jet-stream climatology and
788 typology. *International Journal of Climatology*, 26(3), 283–301.
789 <https://doi.org/10.1002/joc.1255>

- 790 Lee, S., & Kim, H. K. (2003). The dynamical relationship between subtropical and eddy-driven
791 jets. *Journal of the Atmospheric Sciences*, 60(12), 1490–1503. [https://doi.org/10.1175/1520-0469\(2003\)060<1490:TDRBSA>2.0.CO;2](https://doi.org/10.1175/1520-0469(2003)060<1490:TDRBSA>2.0.CO;2)
792
- 793 Li, C., & Wettstein, J. J. (2012). Thermally driven and eddy-driven jet variability in reanalysis.
794 *Journal of Climate*, 25(5), 1587–1596. <https://doi.org/10.1175/JCLI-D-11-00145.1>
- 795 Li, G., & Xie, S. P. (2014). Tropical biases in CMIP5 multimodel ensemble: The excessive
796 equatorial pacific cold tongue and double ITCZ problems. *Journal of Climate*, 27(4), 1765–
797 1780. <https://doi.org/10.1175/JCLI-D-13-00337.1>
- 798 Liebmann, B., & Smith, C. A. (1996). Description of a Complete (Interpolated) Outgoing
799 Longwave Radiation Dataset. *Bulletin of the American Meteorological Society*, 77, 1275–
800 1277.
- 801 Lin, J. L. (2007). The double-ITCZ problem in IPCC AR4 coupled GCMs: Ocean-atmosphere
802 feedback analysis. *Journal of Climate*, 20(18), 4497–4525.
803 <https://doi.org/10.1175/JCLI4272.1>
- 804 Lu, J., Chen, G., & Frierson, D. M. W. (2008). Response of the zonal mean atmospheric
805 circulation to El Niño versus global warming. *Journal of Climate*, 21(22), 5835–5851.
806 <https://doi.org/10.1175/2008JCLI2200.1>
- 807 Maher, P., Kelleher, M. E., Sansom, P. G., & Methven, J. (2020). Is the subtropical jet shifting
808 poleward? *Climate Dynamics*, 54(3–4), 1741–1759. <https://doi.org/10.1007/s00382-019-05084-6>
809
- 810 Mahlstein, I., Martius, O., Chevalier, C., & Ginsbourger, D. (2012). Changes in the odds of
811 extreme events in the Atlantic basin depending on the position of the extratropical jet.
812 *Geophysical Research Letters*, 39(22), 1–6. <https://doi.org/10.1029/2012GL053993>

- Manney, G. L., & Hegglin, M. I. (2018). Seasonal and regional variations of long-term changes in upper-tropospheric jets from reanalyses. *Journal of Climate*, 31(1), 423–448. <https://doi.org/10.1175/JCLI-D-17-0303.1>
- Menzel, M. E., Waugh, D., & Grise, K. (2019). Disconnect Between Hadley Cell and Subtropical Jet Variability and Response to Increased CO₂. *Geophysical Research Letters*, 46(12), 7045–7053. <https://doi.org/10.1029/2019GL083345>
- Nakamura, H. (1992). Midwinter Suppression of Baroclinic Wave Activity in the Pacific. *Journal of Atmospheric Sciences*, 49(17), 1629–1642. [https://doi.org/10.1175/1520-0469\(1992\)049<1629:MSOBWA>2.0.CO;2](https://doi.org/10.1175/1520-0469(1992)049<1629:MSOBWA>2.0.CO;2)
- Panetta, R. L. (1993). Zonal Jets in Wide Baroclinically Unstable Regions: Persistence and Scale Selection. *Journal of the Atmospheric Sciences*, 50(14), 2073–2106. [https://doi.org/10.1175/1520-0469\(1993\)050<2073:ZJIWBU>2.0.CO;2](https://doi.org/10.1175/1520-0469(1993)050<2073:ZJIWBU>2.0.CO;2)
- Petoukhov, V., Rahmstorf, S., Petri, S., & Schellnhuber, H. J. (2013). Quasiresonant amplification of planetary waves and recent Northern Hemisphere weather extremes. *Proceedings of the National Academy of Sciences of the United States of America*, 110(14), 5336–5341. <https://doi.org/10.1073/pnas.1222000110>
- Rodionov, S., & Assel, R. (2001). A new look at the Pacific/North American index. *Geophysical Research Letters*, 28(8), 1519–1522. <https://doi.org/10.1029/2000GL012185>
- Ropelewski, C. F., & Halpert, M. S. (1989). Precipitation Patterns Associated with the High Index Phase of the Southern Oscillation. *Journal of Climate*, 2(3), 268–284. [https://doi.org/10.1175/1520-0442\(1989\)002<0268:PPAWTH>2.0.CO;2](https://doi.org/10.1175/1520-0442(1989)002<0268:PPAWTH>2.0.CO;2)
- Ryoo, J. M., Kaspi, Y., Waugh, D. W., Kiladis, G. N., Waliser, D. E., Fetzer, E. J., & Kim, J. (2013). Impact of Rossby wave breaking on U.S. west coast winter precipitation during

ENSO events. *Journal of Climate*, 26(17), 6360–6382. <https://doi.org/10.1175/JCLI-D-12-00297.1>

Sampe, T., Nakamura, H., Goto, A., & Ohfuchi, W. (2010). Significance of a midlatitude SST frontal zone in the formation of a storm track and an eddy-driven westerly jet. *Journal of Climate*, 23(7), 1793–1814. <https://doi.org/10.1175/2009JCLI3163.1>

Schneider, E. K. (1977). Axially Symmetric Steady-State Models of the Basic State for Instability and Climate Studies. Part II. Nonlinear Calculations. *Journal of the Atmospheric Sciences*, 34(2), 280–296. [https://doi.org/10.1175/1520-0469\(1977\)034<0280:ASSSMO>2.0.CO;2](https://doi.org/10.1175/1520-0469(1977)034<0280:ASSSMO>2.0.CO;2)

Seager, R., Murtugudde, R., Naik, N., Clement, A., Gordon, N., & Miller, J. (2003). Air-sea interaction and the seasonal cycle of the subtropical anticyclones. *Journal of Climate*, 16(12), 1948–1966. [https://doi.org/10.1175/1520-0442\(2003\)016<1948:AIATSC>2.0.CO;2](https://doi.org/10.1175/1520-0442(2003)016<1948:AIATSC>2.0.CO;2)

Smith, S. R., Green, P. M., Leonardi, A. P., & O’Brien, J. J. (1998). Role of Multiple-Level Tropospheric Circulations in Forcing ENSO Winter Precipitation Anomalies. *Monthly Weather Review*, 126(12), 3102–3116. [https://doi.org/10.1175/1520-0493\(1998\)126<3102:ROMLTC>2.0.CO;2](https://doi.org/10.1175/1520-0493(1998)126<3102:ROMLTC>2.0.CO;2)

Solomon, A., Polvani, L. M., Waugh, D. W., & Davis, S. M. (2016). Contrasting upper and lower atmospheric metrics of tropical expansion in the Southern Hemisphere. *Geophysical Research Letters*, 43(19), 10,496–10,503. <https://doi.org/10.1002/2016GL070917>

Son, S. W., & Lee, S. (2005). The response of westerly jets to thermal driving in a primitive equation model. *Journal of the Atmospheric Sciences*, 62(10), 3741–3757.

<https://doi.org/10.1175/JAS3571.1>

- 858 Strong, C., & Davis, R. E. (2007). Winter jet stream trends over the Northern Hemisphere.
859 *Quarterly Journal of the Royal Meteorological Society*, 133(629), 2109–2115.
860 <https://doi.org/10.1002/qj.171>
- 861 Strong, C., & Davis, R. E. (2008). Variability in the position and strength of winter jet stream
862 cores related to northern hemisphere teleconnections. *Journal of Climate*, 21(3), 584–592.
863 <https://doi.org/10.1175/2007JCLI1723.1>
- 864 Wallace, J. M., & Gutzler, D. S. (1981). Teleconnections in the Geopotential Height Field during
865 the Northern Hemisphere Winter. *Monthly Weather Review*, 109(4), 784–812.
866 [https://doi.org/10.1175/1520-0493\(1981\)109<0784:TITGHF>2.0.CO;2](https://doi.org/10.1175/1520-0493(1981)109<0784:TITGHF>2.0.CO;2)
- 867 Waugh, D. W., Grise, K. M., Seviour, W. J. M., Davis, S. M., Davis, N., Adam, O., ... Ming, A.
868 (2018). Revisiting the relationship among metrics of tropical expansion. *Journal of Climate*,
869 31(18), 7565–7581. <https://doi.org/10.1175/JCLI-D-18-0108.1>
- 870 Winters, A. C., & Martin, J. E. (2016). Synoptic and mesoscale processes supporting vertical
871 superposition of the polar and subtropical jets in two contrasting cases. *Quarterly Journal of*
872 *the Royal Meteorological Society*, 142(695), 1133–1149. <https://doi.org/10.1002/qj.2718>
- 873 Woollings, T., Barriopedro, D., Methven, J., Son, S. W., Martius, O., Harvey, B., ... Seneviratne,
874 S. (2018). Blocking and its Response to Climate Change. *Current Climate Change Reports*,
875 4(3), 287–300. <https://doi.org/10.1007/s40641-018-0108-z>
- 876 Woollings, T., Czuchnicki, C., & Franzke, C. (2014). Twentieth century North Atlantic jet
877 variability. *Quarterly Journal of the Royal Meteorological Society*, 140(680), 783–791.
878 <https://doi.org/10.1002/qj.2197>

- 879 Woollings, T., Hannachi, A., & Hoskins, B. (2010). Variability of the North Atlantic eddy-driven
880 jet stream. *Quarterly Journal of the Royal Meteorological Society*, 136(649), 856–868.
881 <https://doi.org/10.1002/qj.625>
- 882 Yu, B., & Lin, H. (2019). Modification of the wintertime Pacific–North American pattern related
883 North American climate anomalies by the Asian–Bering–North American teleconnection.
884 *Climate Dynamics*, 53(1–2), 313–328. <https://doi.org/10.1007/s00382-018-4586-4>
- 885 Yuan, J., Feldstein, S. B., Lee, S., & Tan, B. (2011). The relationship between the North Atlantic
886 jet and tropical convection over the Indian and Western Pacific Oceans. *Journal of Climate*,
887 24(23), 6100–6113. <https://doi.org/10.1175/2011JCLI4203.1>
- 888 Yuval, J., & Kaspi, Y. (2018). Eddy sensitivity to jet characteristics. *Journal of the Atmospheric*
889 *Sciences*, 75(5), 1371–1383. <https://doi.org/10.1175/JAS-D-17-0139.1>
- 890 Zhang, W., & Villarini, G. (2018). Uncovering the role of the East Asian jet stream and
891 heterogeneities in atmospheric rivers affecting the western United States. *Proceedings of the*
892 *National Academy of Sciences of the United States of America*, 115(5), 891–896.
893 <https://doi.org/10.1073/pnas.1717883115>